

Letter

# Seven-Component Model-Based Decomposition for PolSAR Data with Sophisticated Scattering Models

Hui Fan <sup>1,2</sup>, Sinong Quan <sup>1,\*</sup> , Dahai Dai <sup>1</sup>, Xuesong Wang <sup>1</sup> and Shunping Xiao <sup>1</sup>

<sup>1</sup> State Key Laboratory of Complex Electromagnetic Environment Effects on Electronics and Information System, National University of Defense Technology, Changsha 410073, Hunan, China; fanhui17@nudt.edu.cn (H.F.); daidahai@nudt.edu.cn (D.D.); wangxuesong@nudt.edu.cn (X.W.); xiaoshunping@nudt.edu.cn (S.X.)

<sup>2</sup> College of Computer and Information Engineering, Central South University of Forestry and Technology, Changsha 410004, Hunan, China

\* Correspondence: quansinong13@nudt.edu.cn; Tel.: +86-132-9865-7814

Received: 25 September 2019; Accepted: 26 November 2019; Published: 27 November 2019



**Abstract:** Due to incomprehensive and inaccurate scattering modeling, the state-of-the-art polarimetric synthetic aperture radar (PolSAR) model-based target decompositions are incapable of effectively depicting the scattering mechanism of obliquely oriented urban areas. In this paper, a seven-component model-based decomposition scheme is proposed by constructing several sophisticated scattering models. First, an eigenvalue-based obliquely-oriented dihedral scattering model is presented to reasonably distribute the co-polarization and cross-polarization scattering powers in obliquely oriented urban areas, thus accurately characterizing the urban scattering. Second, the  $\pm 45^\circ$  oriented dipole and  $\pm 45^\circ$  quarter-wave reflector scattering models are incorporated for the purpose of accounting for the real and imaginary components of the  $T_{13}$  element in the coherency matrix so as to fully utilize polarimetric information. Finally, according to their mathematical forms, several strategies for model parameter solutions are designed, and the seven-component decomposition is fulfilled. Experimental results conducted on different PolSAR data demonstrate that the proposed method considerably improves the PolSAR scattering interpretation in a more physical manner compared to other existing model-based decomposition, which can be applied for urban area detection, classification, and other urban planning applications.

**Keywords:** polarimetric synthetic aperture radar (PolSAR); seven-component model-based decomposition; obliquely oriented dihedral scattering model;  $\pm 45^\circ$  oriented dipole scattering model;  $\pm 45^\circ$  oriented quarter-wave reflector scattering model

## 1. Introduction

The polarimetric synthetic aperture radar (PolSAR) model-based decomposition (MBD) technique has attracted continuous attention since it plays an important role in PolSAR image interpretation [1–5]. With the MBD techniques, a received radar return signal can be separated into a sum of various scattering contributions, which allows one to regain a better insight into the physics underlying the original measured matrix [6–11]. By introducing the physical scattering model, the MBD can accelerate the interpretation of the scattering mechanism and promote the visualized presentation of the PolSAR image considerably.

Advancements in the MBD and its application to civil and military remote sensing fields have increased manifolds and resulted in numerous researches in recent decades. The most fundamental concept of three-component decomposition was introduced by Freeman (F3D) under the assumption of reflection symmetry [1]. To deal with the non-reflection symmetric case, Yamaguchi et al. [2]

constructed four-component decomposition (Y4D) by adding the helix scattering model, which is relevant for describing man-made targets in urban area scattering.

In the past two decades, most of the MBD methods have been developed on the basis of the F3D and Y4D methods. Part of these methods adopted the mathematical operations, i.e., non-negative eigenvalue decomposition (NNED) [12–14] and orientation angle compensation (OAC) [15–19], for the input coherency matrix to estimate the scattering contributions in order to pursue an accurate scattering interpretation in a mathematical manner. Despite this, researches are more inclined to introduce sophisticated scattering models to develop and improve the MBD in a physical manner. For instance, to describe the cross-pol scattering component induced by double-bounce structures and reduce the overestimation of volume scattering (OVS), Sato et al. [20] defined a rotated dihedral scattering model and incorporated it into the Y4D (S4R). By introducing the wire scattering model related with the cross-pol scattering component, Zhang et al. [21] innovatively proposed a five-component decomposition scheme that can better describe complicated shapes of man-made structures in urban areas. Inspired by the thought of five-component decomposition, Xiang et al. [22] further constructed a cross scattering model (CSM) to emphasize the cross-pol scattering component especially caused by buildings with oblique orientations (OOBs). In general, these MBD methods offered straightforward interpretation for scattering mechanisms and have met with different degrees of success in extracting the corresponding scattering characteristics in PolSAR images. Despite all this, there still exist certain drawbacks to these methods. On the one hand, subject to certain assumptions, these methods have lost important polarimetric information (the real and imaginary part of the  $T_{13}$  term) in the coherency matrix. On the other hand, these methods are designed for specific application scenarios (e.g., F3D for naturally occurring scatterers), which are not applicable to the general conditions.

Recently, Singh et al. proposed a six-component decomposition (S6D) [23], in which the procedure is implemented by introducing the  $\pm 45^\circ$  oriented dipole (OD) and  $\pm 45^\circ$  oriented quarter-wave reflector (OQW) scattering models to respectively account for the real and imaginary parts of the  $T_{13}$  term. This not only guarantees the further utilization of polarimetric information but also releases the restriction of reflection symmetry assumption. However, the method still suffers the deficiencies in several aspects. First, the model used for describing the cross-pol scattering components produced by rotated dihedral scattering is essentially inappropriate because the matrix elements are approximately equal [20]. Second, the overall rotated dihedral scattering is considered as volume scattering. These may both lead to the OVS and scattering mechanism ambiguity.

To address the aforementioned issues, a seven-component decomposition scheme by constructing several sophisticated scattering models is proposed in this paper. The main work includes the following aspects. First, to overcome the OVS and reasonably distribute the co-polarization and cross-polarization scattering powers in OOBs, an obliquely oriented dihedral (OOD) scattering model is proposed. Second, to account for non-reflection symmetry and to further utilize polarimetric information, the  $\pm 45^\circ$  OD and  $\pm 45^\circ$  OQW scattering models in [23] are incorporated. Along with the OOD scattering model, the whole decomposition procedure is extended to a seven-component decomposition scheme from the original Y4D. Finally, an exquisite model parameter solution is designed according to the mathematical forms of these sophisticated scattering models, and the seven-component decomposition is accomplished. Different PolSAR data are utilized to verify the effectiveness of the proposed method. The results demonstrate that the proposed method considerably improves the PolSAR scattering interpretation ability and outperforms the state-of-the-art MBDs in a more physical manner.

## 2. Methodology

### 2.1. Basic Scattering Model

Under the circumstance of the reciprocity condition, the measured coherency matrix can be presented as

$$\langle [T] \rangle = \langle k_{3p} k_{3p}^H \rangle = \begin{bmatrix} T_{11} & T_{12} & T_{13} \\ T_{21} & T_{22} & T_{23} \\ T_{31} & T_{32} & T_{33} \end{bmatrix} \quad (1)$$

where  $k_{3p}$  represents the Pauli vector. The superscript H and the notation  $\langle \rangle$  indicate the conjugate transpose and ensemble averaging, respectively. In the Y4D, the coherency matrix is decomposed as a weighted sum of four kinds of basic scattering, i.e., surface, double-bounce, helix and volume scattering, which is given as

$$\langle [T] \rangle = f_S [T]_S + f_D [T]_D + f_H [T]_H + f_V [T]_V \quad (2)$$

where  $f_S$ ,  $f_D$ ,  $f_H$ , and  $f_V$  are scattering coefficients to be computed.  $[T]_S$ ,  $[T]_D$ ,  $[T]_H$  and  $[T]_V$  are the models of surface, double-bounce, helix, and volume scattering in the Y4D [2], respectively. Their mathematical forms are given as

$$[T]_S = \begin{bmatrix} 1 & \beta^* & 0 \\ \beta & |\beta|^2 & 0 \\ 0 & 0 & 0 \end{bmatrix}, [T]_D = \begin{bmatrix} |\alpha|^2 & \alpha & 0 \\ \alpha^* & 1 & 0 \\ 0 & 0 & 0 \end{bmatrix} \quad (3)$$

$$[T]_H = \frac{1}{2} \begin{bmatrix} 0 & 0 & 0 \\ 0 & 1 & \pm j \\ 0 & \mp j & 1 \end{bmatrix}, [T]_V = \frac{1}{4} \begin{bmatrix} 2 & 0 & 0 \\ 0 & 1 & 0 \\ 0 & 0 & 1 \end{bmatrix}.$$

Thereinto,  $\alpha$  and  $\beta$  denote the model parameters of double-bounce scattering and surface scattering, respectively.  $j$  represents the imaginary unit, and the positive (negative) sign indicates right (left) helix scattering.

### 2.2. Sophisticated Scattering Model

#### 2.2.1. OOD Scattering Model

Cross-pol responses not only significantly occur in natural areas but also in OOBs, whose main scattering centers are at an oblique direction with respect to the radar illumination [24–28]. Traditional MBDs generally assign the overall cross-pol components to volume scattering, which results in severe OVS and scattering mechanism ambiguity; thus, the discrimination between OOBs and natural areas is difficult to make. To separate the cross-pol components caused by oriented dihedrals from the overall cross-pol components, Xiang et al. proposed the well-known cross scattering model, which is formed from a rotated dihedral structure considering its orientation angle [22]. However, there exist some intrinsic drawbacks in the CSM in that it includes an approximately equal amount of co-pol component (the  $T_{22}$  term) and cross-pol component (the  $T_{33}$  term) according to its algebraic model [22,29]. Meanwhile, in the actual OOB regions, it is observed that cross-pol power is more intense than co-pol power [24–28]. Inspired by this, this section proposes a modified version of the CSM (OOD scattering model), which conforms more to reality. The modified principle we need to follow is that the  $T_{33}$  term should be much larger than the  $T_{22}$  term, so as to ensure that the cross-polarization component is larger than the co-polarization component. Meanwhile, the proposed model adopts the

same matrix form with the CSM since this matrix form can effectively distribute the overall cross-pol components. Accordingly, the proposed OOD scattering has the following form:

$$[\mathbf{T}]_{\text{OOD}} = \begin{bmatrix} 0 & 0 & 0 \\ 0 & O_{22} & 0 \\ 0 & 0 & O_{33} \end{bmatrix} \quad (4)$$

where

$$O_{22} = \frac{F_{\text{OOD}}}{F_{\text{OOD}} + \frac{F_{\text{OOD}}}{\max(F_{\text{OOD}}) - F_{\text{OOD}} + \xi}}, O_{33} = \frac{\frac{F_{\text{OOD}}}{\max(F_{\text{OOD}}) - F_{\text{OOD}} + \xi}}{F_{\text{OOD}} + \frac{F_{\text{OOD}}}{\max(F_{\text{OOD}}) - F_{\text{OOD}} + \xi}}. \quad (5)$$

where  $F_{\text{OOD}}$  is a modified factor to be determined, and  $\xi$  is an infinitesimally small positive number that prevents the denominator from becoming zero. The rational of the above modification lies in that  $A/[\max(A) - A]$  is always significantly larger than  $A$  if the range of  $A$  is  $[0, 1]$ . Thus, the factor  $F_{\text{OOD}}$  should be a feature associated with the scattering characteristics of OOBs, while its value ranges from 0 to 1. In this case, our newly proposed OOB descriptor is considered [30], which is constructed based on the following facts.

(1) In real applications, a large cross-polarization component closely relates to remarkable scattered energy depolarization [30], and the completely depolarized component of the total power can be measured by the minimum eigenvalue  $\lambda_3$ . The radar return is completely polarized when  $\lambda_3 = 0$  and the depolarized component increases with the increment of  $\lambda_3$  [30]. Consequently, the value of  $\lambda_3$  in OOBs is high.

(2) Due to the oblique orientation, double reflection signals from OOBs no longer travel back to the radar. This leads to other direct reflections from the ground that begin to dominate, and random signals appear [30]. As a result, the scattering randomness of OOBs is high.

(3) It is observed that buildings approximately aligned with the flight trajectory (AABs) and natural targets generate medium and high polarimetric asymmetry, respectively [31]. However, OOBs generate low polarimetric asymmetry [31].

Accordingly, the expression of  $F_{\text{OOD}}$  is

$$F_{\text{OOD}} = M_{\text{DP}} \cdot M_{\text{RD}} \cdot (1 - M_{\text{PA}})^2 = \lambda_3 \cdot \frac{4\lambda_3}{\text{SPAN}} \cdot \left(1 - \frac{\lambda_1 - \lambda_2}{\text{SPAN} - 3\lambda_3}\right)^2 \quad (0 < F_{\text{OOD}} < 1) \quad (6)$$

where SPAN is total power of the radar return and  $\lambda_i (i = 1, 2, 3)$  are the eigenvalues of the coherency matrix [31].  $M_{\text{DP}}$ ,  $M_{\text{RD}}$ , and  $M_{\text{PA}}$  are the measurements of depolarization, randomness, and polarimetric asymmetry, respectively [30].  $M_{\text{DP}}$  measures the completely depolarized component of the total power.  $M_{\text{RD}}$  denotes the radar vegetation index, which serves to measure the randomness in polarization signatures. Meanwhile,  $M_{\text{PA}}$  is the measurement of the relative strength of the two scattering processes. It should be noted that  $F_{\text{OOD}}$  is defined as the product of these three measurements rather than the addition because the values of these measurements are not on the same level.

Compared with the CSM, the OOD scattering model is optimized in two aspects. First, to represent a certain amount of co-pol components in OOBs, the original  $T_{22}$  term in [22] is substituted with  $F_{\text{OOD}}$  without any prior information. Then, in view of the cross-pol components in OOBs, the original  $T_{33}$  term in [22] is substituted with  $F_{\text{OOD}}/(\max(F_{\text{OOD}}) - F_{\text{OOD}})$ . Regardless of the value of  $F_{\text{OOD}}$ ,  $F_{\text{OOD}}/(\max(F_{\text{OOD}}) - F_{\text{OOD}})$  is always greater than  $F_{\text{OOD}}$ , which makes the relative proportion of co-polarization and cross-polarization components conform more to reality. Finally, the matrix elements are rigorously normalized to  $[0, 1]$ . Through the above modifications, the cross-polarization components are significantly elevated, such that the approximations are more reasonable, and the OOD scattering model aligns with the actuals with more certainty.

### 2.2.2. $\pm 45^\circ$ Oriented Dipole and Quarter-Wave Reflector Scattering Models

Without the unitary transformation, the majorities of MBDs separate the received radar return signal into a sum of various scattering components by utilizing at most six out of nine independent observations (i.e., the  $T_{11}$ ,  $T_{22}$ ,  $T_{33}$ , the real part of  $T_{12}$ , the imaginary part of  $T_{12}$  and the imaginary part of  $T_{23}$  terms) in the coherency matrix. Nevertheless, the  $T_{13}$  term has not been utilized for corresponding to additional scattering components. It has been proved that the coherency matrix does not obey the reflection symmetry assumption in many complex natural (forest, orchard, mountainous terrain, etc.) and man-made (urban areas, etc.) scattering scenarios [23]. Therefore, to enhance the utilization of polarimetric information and to release the restriction of reflection symmetry assumption, one should integrate the  $T_{13}$  term into the MBD through appropriate scattering modeling.

To this end, the  $\pm 45^\circ$  OD and  $\pm 45^\circ$  OQW scattering models [23] are incorporated to account for the real part of  $T_{13}$  and the imaginary part of  $T_{13}$  terms, the corresponding physical configurations are illustrated in Figure 1. For dipoles oriented at  $45^\circ$  and  $-45^\circ$ , as shown in Figure 1a, the corresponding scattering matrices are expressed in the following equations:

$$\begin{aligned} [\mathbf{S}]_{\text{OD}}^{45^\circ} &= [\mathbf{S}]_1 = \begin{bmatrix} 1 & 1 \\ 1 & 1 \end{bmatrix} \\ [\mathbf{S}]_{\text{OD}}^{-45^\circ} &= [\mathbf{S}]_2 = \begin{bmatrix} 1 & -1 \\ -1 & 1 \end{bmatrix}. \end{aligned} \quad (7)$$

Accordingly, the coherency matrix of  $\pm 45^\circ$  OD scattering model can be obtained by the inner product of Pauli vectors of the scattering matrix, which has the following form [23]:

$$[\mathbf{T}]_{\text{OD}}^{\pm 45^\circ} = \frac{1}{2} \begin{bmatrix} 1 & 0 & \pm 1 \\ 0 & 0 & 0 \\ \pm 1 & 0 & 1 \end{bmatrix}. \quad (8)$$

For  $\pm 45^\circ$  OQW scattering model, as shown in Figure 1b, the scattering matrix can be obtained by the summation of scattering matrices of the  $\pm 45^\circ$  oriented dipoles locating at different distances, which is expressed by [23]

$$\begin{aligned} [\mathbf{S}]_{\text{OQW}}^{45^\circ} &= [\mathbf{S}]_1 + [\mathbf{S}]_2 P(0) + [\mathbf{S}]_2 P\left(\frac{\lambda}{8}\right) + [\mathbf{S}]_1 P\left(\frac{3\lambda}{8}\right) = \begin{bmatrix} 1 & j \\ j & 1 \end{bmatrix} \\ [\mathbf{S}]_{\text{OQW}}^{-45^\circ} &= [\mathbf{S}]_1 + [\mathbf{S}]_2 P(0) + [\mathbf{S}]_1 P\left(\frac{\lambda}{8}\right) + [\mathbf{S}]_2 P\left(\frac{3\lambda}{8}\right) = \begin{bmatrix} 1 & -j \\ -j & 1 \end{bmatrix} \end{aligned} \quad (9)$$

where  $P(d) = \exp(-j(4\pi d/\lambda))$  is phase delay generated by spacing  $d$  and can be given in the following equation [23]

$$P(d) = \begin{cases} 1, & \text{when } d = 0 \\ -j, & \text{when } d = \frac{\lambda}{8} \\ -1, & \text{when } d = \frac{2\lambda}{8} = \frac{\lambda}{4} \\ j, & \text{when } d = \frac{3\lambda}{8}. \end{cases} \quad (10)$$

In a similar manner, the coherence matrix of  $\pm 45^\circ$  OQW scattering model is obtained from the scattering matrix, which is expressed in the following

$$[\mathbf{T}]_{\text{OQW}}^{\pm 45^\circ} = \frac{1}{2} \begin{bmatrix} 1 & 0 & \mp j \\ 0 & 0 & 0 \\ \pm j & 0 & 1 \end{bmatrix}. \quad (11)$$

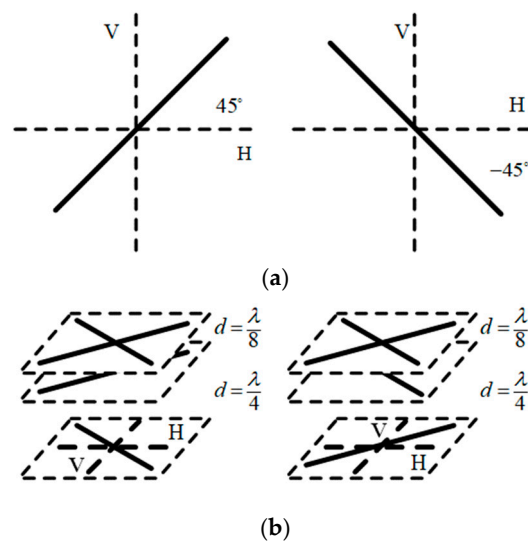


**Figure 1.** Physical configurations. (a)  $\pm 45^\circ$  oriented dipoles. (b)  $\pm 45^\circ$  oriented quarter-wave reflectors.

It is intuitive that the  $\pm 45^\circ$  OD and  $\pm 45^\circ$  OQW scattering models are coherent since their ranks both equal to 1. For the MBD, in principle, we are free to choose arbitrary decomposition terms, but in practice, there are several constraining factors. The first is recognition of the fact that each composite matrix must have at least one free element to describe its form and structure [32]. On the other hand, it can be seen that a coherency matrix has at most nine free elements. Therefore, in most backscatter applications, the coherency matrix can be decomposed into nine terms at most.

As a matter of fact, due to the certain limiting factors and insufficient utilization of polarimetric information, the fit gap between the input matrix and the scattering model in the MBD always exists, which results in the generation of residual components more or less. In the traditional MBDs,  $\pm 45^\circ$  OD and  $\pm 45^\circ$  OQW scattering correspond to their residual components. Meanwhile, in our proposed decomposition scheme, these two scatterings are separately distilled and regarded as new scattering components, which exist widely in oriented urban areas, vegetation areas, and sloped surfaces [23].

### 2.3. Model Solution

According to the OOD,  $\pm 45^\circ$  OD, and  $\pm 45^\circ$  OQW scattering models, the proposed seven-component decomposition is presented as the weighted sum of several basic scattering, i.e.,

$$\langle [T] \rangle = f_S [T]_S + f_D [T]_D + f_H [T]_H + f_V [T]_V + f_{OOD} [T]_{OOD} + f_{OD} [T]_{OD} + f_{OQW} [T]_{OQW} \quad (12)$$

where  $f_{OOD}$ ,  $f_{OD}$ , and  $f_{OQW}$  are the corresponding scattering coefficients. Based on the aforementioned models, one set of equations can be achieved, i.e.,

$$\begin{aligned} f_S + f_D |\alpha|^2 + \frac{f_V}{2} + \frac{f_{OD}}{2} + \frac{f_{OQW}}{2} &= T_{11} \\ f_S |\beta|^2 + f_D + \frac{f_V}{4} + \frac{f_H}{2} + f_{OOD} O_{22} &= T_{22} \\ \frac{f_V}{4} + \frac{f_H}{2} + f_{OOD} O_{33} + \frac{f_{OD}}{2} + \frac{f_{OQW}}{2} &= T_{33} \\ f_S \beta^* + f_D \alpha &= T_{12} \\ \frac{f_H}{2} &= |\text{Im}(T_{23})| \\ \frac{f_{OD}}{2} &= \text{Re}(T_{13}) \\ \frac{f_{OQW}}{2} &= |\text{Im}(T_{13})| \end{aligned} \quad (13)$$

It is apparent that Equation (13) consists of nine unknowns and eight observations. To deal with the underdetermined issue, it is necessary to make assumptions so as to reduce the unknowns. According to the sign of  $T_{11} - T_{22} + f_H/2 - f_{OD}/2 - f_{OQW}/2$ , one of the unknowns can be fixed.

If  $T_{11} - T_{22} + f_H/2 - f_{OD}/2 - f_{OQW}/2 > 0$ , then  $f_D = 0$ , assuming the surface scattering dominates in the remaining matrix (subtracting the helix,  $\pm 45^\circ$  OD, and  $\pm 45^\circ$  OQW scattering components from the input coherency matrix), otherwise  $f_S = 0$ , assuming the double-bounce scattering dominates in the remaining matrix. Moreover, although the expressions in (13) are compact, it is difficult to achieve the analytic solutions directly. On the one hand, under the case of small  $F_{OOD}$ , the  $f_{OOD}O_{22}$  term can be negligible. On the other hand, the normalization also make  $f_{OOD}O_{22}$  ignorable while  $F_{OOD}$  approaches its maximum value. As a result, the equations become solvable, and the following formula can be obtained with modular calculation:

$$\begin{aligned} T_{11} - T_{22} + \frac{f_H}{2} - \frac{f_{OD}}{2} - \frac{f_{OQW}}{2} > 0 : \text{Re}(\beta) &= \frac{\text{Re}(T_{12})}{f_S}, \text{Im}(\beta) = \frac{-\text{Im}(T_{12})}{f_S} \\ T_{11} - T_{22} + \frac{f_H}{2} - \frac{f_{OD}}{2} - \frac{f_{OQW}}{2} < 0 : \text{Re}(\alpha) &= \frac{\text{Re}(T_{12})}{f_D}, \text{Im}(\alpha) = \frac{\text{Im}(T_{12})}{f_D}. \end{aligned} \tag{14}$$

Through combing Equations (13) and (14), we can get

$$\begin{aligned} T_{11} - T_{22} + \frac{f_H}{2} - \frac{f_{OD}}{2} - \frac{f_{OQW}}{2} > 0 : f_S^2 + (2T_{22} - f_H - T_{11} + \frac{f_{OD}}{2} + \frac{f_{OQW}}{2})f_S - 2|T_{12}|^2 &= 0 \\ T_{11} - T_{22} + \frac{f_H}{2} - \frac{f_{OD}}{2} - \frac{f_{OQW}}{2} < 0 : 2f_D^2 + (T_{11} + f_H - 2T_{22} - \frac{f_{OD}}{2} - \frac{f_{OQW}}{2})f_D - |T_{12}|^2 &= 0. \end{aligned} \tag{15}$$

The discriminants of the two quadratic equations in Equation (15) are given as:

$$\begin{aligned} T_{11} - T_{22} + \frac{f_H}{2} - \frac{f_{OD}}{2} - \frac{f_{OQW}}{2} > 0 : \Delta &= (T_{22} - \frac{T_{11}}{2} - \frac{f_H}{2} + \frac{f_{OD}}{4} + \frac{f_{OQW}}{4})^2 + 2|T_{12}|^2 \\ T_{11} - T_{22} + \frac{f_H}{2} - \frac{f_{OD}}{2} - \frac{f_{OQW}}{2} < 0 : \Delta &= (T_{11} - 2T_{22} + f_H - \frac{f_{OD}}{2} - \frac{f_{OQW}}{2})^2 + 8|T_{12}|^2. \end{aligned} \tag{16}$$

It is apparent that the quadratic discriminants in (16) are always positive; there are two roots for the quadratic equation. Accordingly, there are three possible solutions: (1) if the larger root is negative,  $f_S$  (or  $f_D$ ) is forced to zero; (2) if the larger root is positive and the smaller root is negative,  $f_S$  (or  $f_D$ ) is equal to the larger root; and (3) if the smaller root is positive,  $f_S$  (or  $f_D$ ) still equals the larger root. This restricts the overestimation of the volume scattering contribution.

Upon the determination of the surface or double-bounce scattering coefficient, the rest scattering coefficients can be calculated. Their expressions are given as

$$\begin{aligned} T_{11} - T_{22} + \frac{f_H}{2} - \frac{f_{OD}}{2} - \frac{f_{OQW}}{2} > 0 : f_D &= 0, f_H = 2|\text{Im}(T_{23})| \\ f_S &= \frac{\pm \sqrt{(2T_{22} - f_H - T_{11} + \frac{f_{OD}}{2} + \frac{f_{OQW}}{2})^2 + 8|T_{12}|^2} - (2T_{22} - f_H - T_{11} + \frac{f_{OD}}{2} + \frac{f_{OQW}}{2})}{2} \\ f_V &= 2(T_{11} - f_S - \frac{f_{OD}}{2} - \frac{f_{OQW}}{2}), f_{OOD} = \frac{4T_{33} - 2f_H - f_V - 2f_{OD} - 2f_{OQW}}{4O_{33}}. \end{aligned} \tag{17}$$

or

$$\begin{aligned} T_{11} - T_{22} + \frac{f_H}{2} - \frac{f_{OD}}{2} - \frac{f_{OQW}}{2} < 0 : f_S &= 0, f_H = 2|\text{Im}(T_{23})| \\ f_D &= \frac{\pm \sqrt{(T_{11} + f_H - 2T_{22} - \frac{f_{OD}}{2} - \frac{f_{OQW}}{2})^2 + 8|T_{12}|^2} - (T_{11} + f_H - 2T_{22} - \frac{f_{OD}}{2} - \frac{f_{OQW}}{2})}{4} \\ f_V &= 2(2T_{22} - 2f_D - f_H), f_{OOD} = \frac{4T_{33} - 2f_H - f_V - 2f_{OD} - 2f_{OQW}}{4O_{33}}. \end{aligned} \tag{18}$$

As a result, for the purpose of power conservation, the corresponding scattering contributions  $P_S, P_D, P_H, P_V, P_O, P_{OD}, P_{OQW}$  are estimated as

$$\begin{aligned} P_S &= f_S(1 + |\beta|^2), P_D = f_D(1 + |\alpha|^2), P_H = f_H, P_{OOD} = f_{OOD}, P_{OD} = f_{OD}, P_{OQW} = f_{OQW} \\ P_V &= \text{SPAN} - P_S - P_D - P_H - P_{OOD} - P_{OD} - P_{OQW}. \end{aligned} \tag{19}$$

The flowchart of the proposed seven-component decomposition is shown in Figure 2.

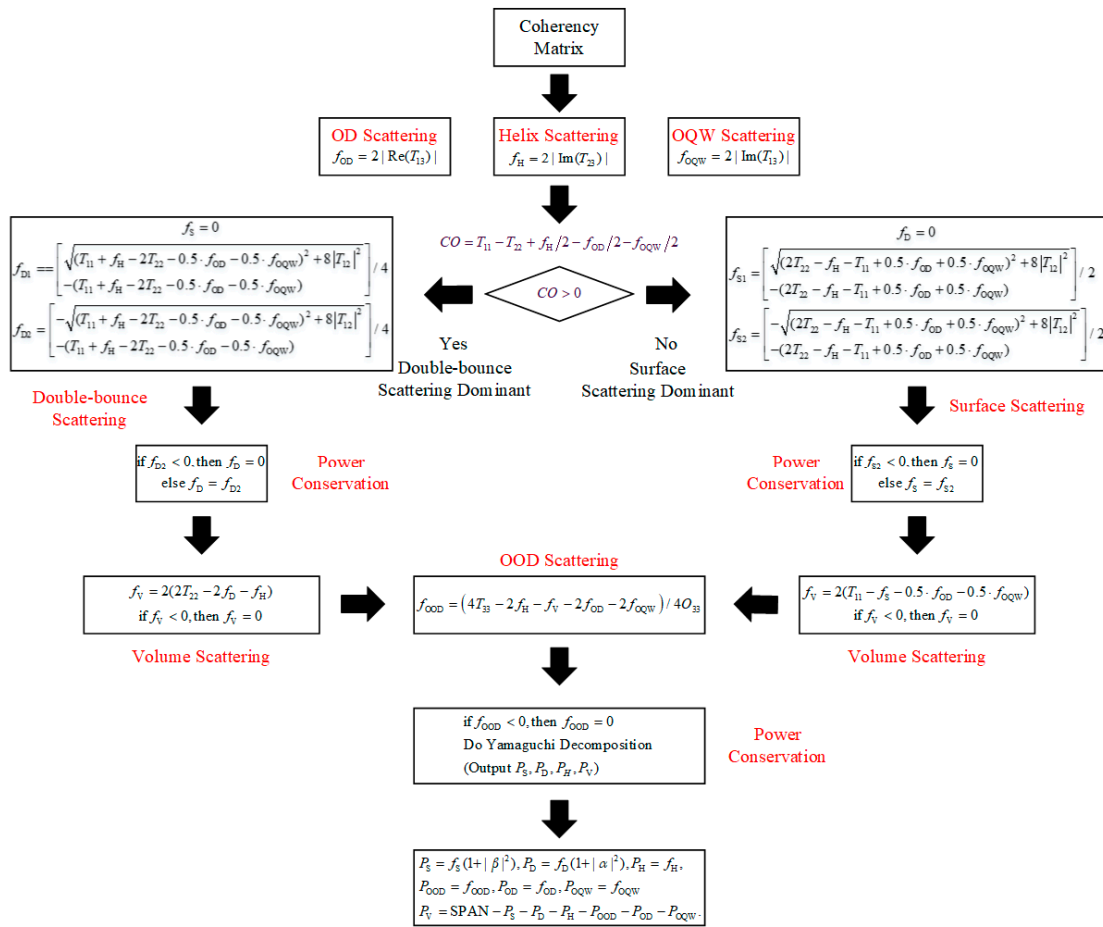


Figure 2. The flowchart of the proposed seven-component decomposition.

### 3. Experimental Results

#### 3.1. Data Description

To evaluate the performance of the proposed seven-component decomposition method, the results reported here are derived from different PolSAR data. The first study data is ALOS PALSAR L-band data acquired over a test site in Hiroshima, Japan, on 16 November 2008. The second study data is Radarsat-2 C-band data acquired in San Francisco, USA, on 9 April 2008. All original PolSAR data are single-look complex. The pixel resolution of ALOS PALSAR L-band data is about  $3.53 \times 9.37$  m. For the Radarsat-2 C-band data, it has a resolution with 4.82 and 4.73 m in the azimuth and range direction, respectively.

Figure 3 displays the Pauli color-coded images for the ALOS PALSAR L-band and Radarsat-2 C-band data. The corresponding optical images are also presented in Figure 3, which are used as the ground references. It can be seen that various types of urban landforms are included ranging from buildings with different orientations to forests and oceans. As a result, the effectiveness of the proposed method can be adequately evaluated.

#### 3.2. Decomposition Results on L-Band Data

To comprehensively evaluate the decomposition performance, four decomposition methods from different aspects, i.e., the S6D [23], the X5D [22], the S4R [20], and the Y4D [2] are involved in the comparison. The color composite results of these methods are shown in Figure 4, where the red channel denotes urban scattering (the sum of double-bounce, helix, the OOD/cross scattering, the  $\pm 45^\circ$  OD and  $\pm 45^\circ$  OQW scattering), the green channel denotes volume scattering, and the blue channel denotes

surface scattering. Moreover, the decomposed seven scattering components from the proposed method are given in Figure 5. In addition to these, the cross scattering,  $\pm 45^\circ$  OD, and  $\pm 45^\circ$  OQW scattering components from the X5D and 6SD methods are further presented in Figure 6 for a comparison.

Overall, the dominant scattering mechanism in ocean areas is surface scattering, which is reflected in blue in the color composite results, while the volume scattering is dominated in forest areas, which is shown by green. On inspection, it is clear that compared with the results of the Y4D, the green tones in the OOBs are less distinct with the S4R (as shown in Figure 4b). This could be attributed to the adoption of rotation dihedral scattering model and the OAC in the S4R; thus, the volume scattering is reduced. With respect to the X5D, the amplitude of yellow components in the OOBs is higher than that of the S4R. This is due to the fact that the cross scattering components are prominent in the concerned region because the X5D can effectively separate the cross-polarization responses caused by OOBs from the overall cross-polarization responses. Although the S6D does not consider the cross scattering, the results in OOBs are still darker in yellow compared with the X5D. This can be interpreted in that the  $\pm 45^\circ$  OD and  $\pm 45^\circ$  OQW scattering models can distribute more cross-polarization components versus the CSM. In contrast, the results in the proposed method exhibit intense red tones in OOBs. This indicates that the corresponding urban scattering is the strongest such that the OVS is improved to the greatest extent.

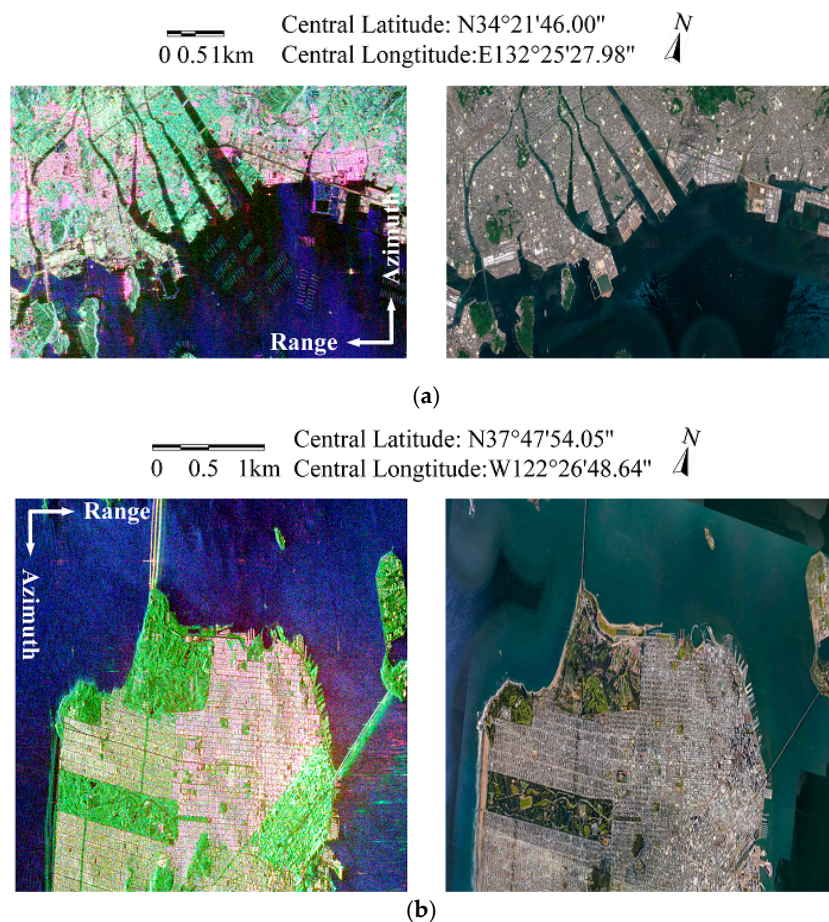


**Figure 3.** Pauli color-coded images and the corresponding optical images. (a) ALOS PALSAR L-band data. (b) Radarsat-2 C-band data.

From Figures 4–6, it can be seen that the  $\pm 45^\circ$  OD and  $\pm 45^\circ$  OQW scattering are widespread in natural areas. This is reasonable because the  $T_{13}$  term is not strictly equal to zero, even though the reflection symmetry is expected. In addition, these components are distributed in sloped surfaces as well [23]. What is noteworthy is that the  $\pm 45^\circ$  OD and  $\pm 45^\circ$  OQW scattering in OOBs are obviously

highlighted and stay at a higher level compared with AABs (outlined by the red circles in Figures 5 and 6). As generally known, for AABs whose dominant scattering mechanism is double-bounce scattering, the dihedral structure is considered to be a symmetric target [25]. Whereas regarding OOBs, the reflection symmetry of these buildings is often broken because significant cross-polarization powers are induced. In this case, the magnitudes of the  $T_{13}$  term in OOBs are remarkably larger than those in AABs, leading to more intense  $\pm 45^\circ$  OD and  $\pm 45^\circ$  OQW scattering. This reveals that the  $\pm 45^\circ$  OD and  $\pm 45^\circ$  OQW scattering models can effectively account for the  $T_{13}$  term, hence further utilizing the polarimetric information.

On the other hand, it is clear that the OOD scattering component is remarkable in OOBs but inconspicuous in other areas. Moreover, the OOD scattering power increases along with the building orientation. In contrast, although the cross scattering component can also sketch the building contours, its distributions are more sporadic, and its power is weaker (outlined by the yellow rectangles). The reason is that the cross-polarization and co-polarization components are reasonably assigned in the OOD scattering model. This enables the OOD scattering model to describe the cross-polarization responses better and thus moderate the OVS.

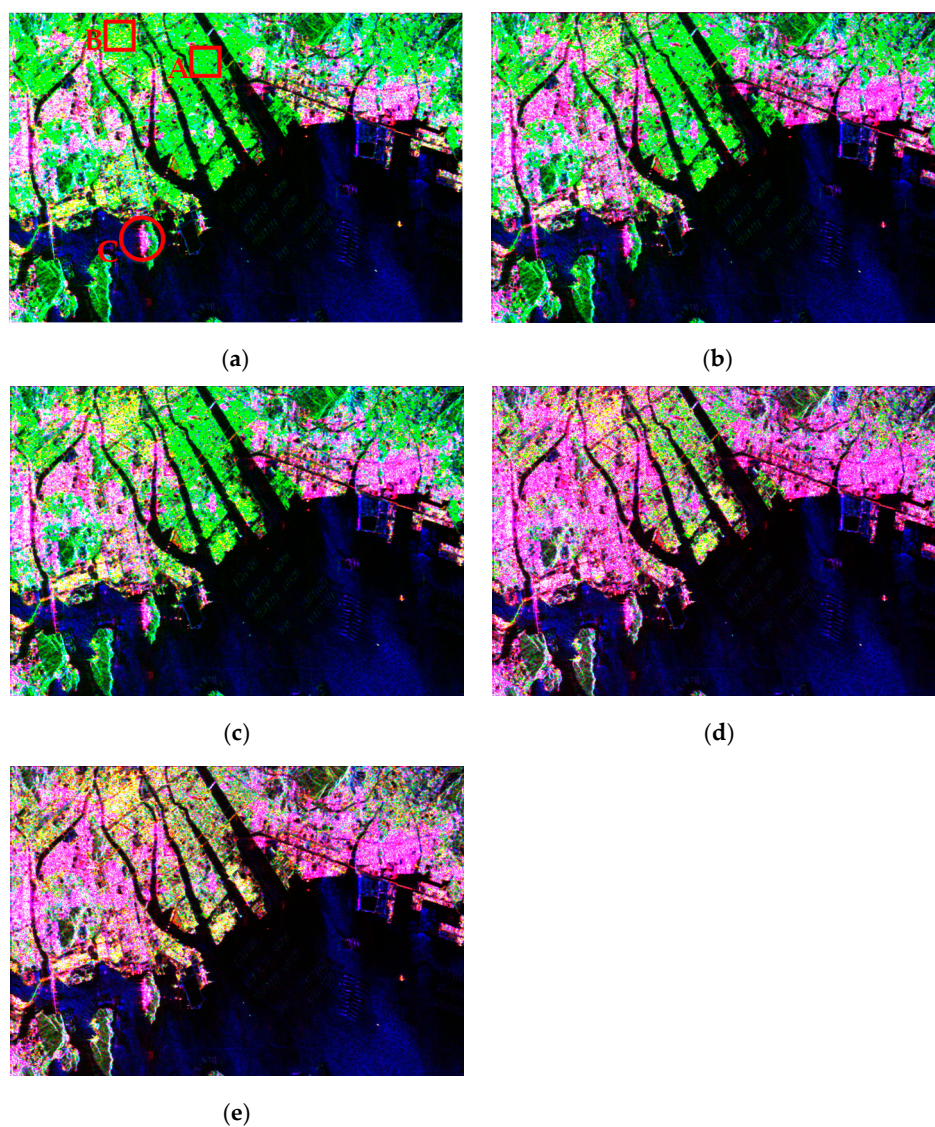


**Figure 4.** Decomposition results for L-band data. (a–e) Color composite results of the Y4D, S4R, X5D, S6D, and the proposed method. (red: urban scattering, green: volume scattering, blue: surface scattering).

To quantitatively compare the performances of these decomposition methods, two different regions (the red rectangular regions A and B in Figure 4a) are selected for further analysis. Regions A and B are OOBs with different orientations, their corresponding topologies are shown in Figure 7. The corresponding normalized scattering power statistics are shown in Tables 1 and 2. It can be seen that surface scattering power gradually increases from the Y4D to the proposed method, and it accounts for a certain proportion in the proposed statistics. This can be interpreted as odd-bounce returns from roofs, streets, and structures between two buildings, which are reasonable and conform to reality.

In OOBs, the double-bounce scattering power is expected to be weak, whereas its proportion is the largest in the S6D, among other methods. This can be explained that the OAC involved in the S6D can transfer part of the cross-polarization power (the  $T_{33}$  term) to the co-polarization power (the  $T_{22}$  term), therefore enhancing the double-bounce scattering. It is noteworthy that the OOD scattering power in region B is almost twice as much as the cross scattering power (4.68% versus 2.65%). This explains that through reasonably distributing the co-polarization and cross-polarization components, the proposed method can not only preserve but also enhance the cross-pol scattering power in OOBs. In this case, the urban scattering can be characterized with more certainty by further emphasizing the OOD scattering.

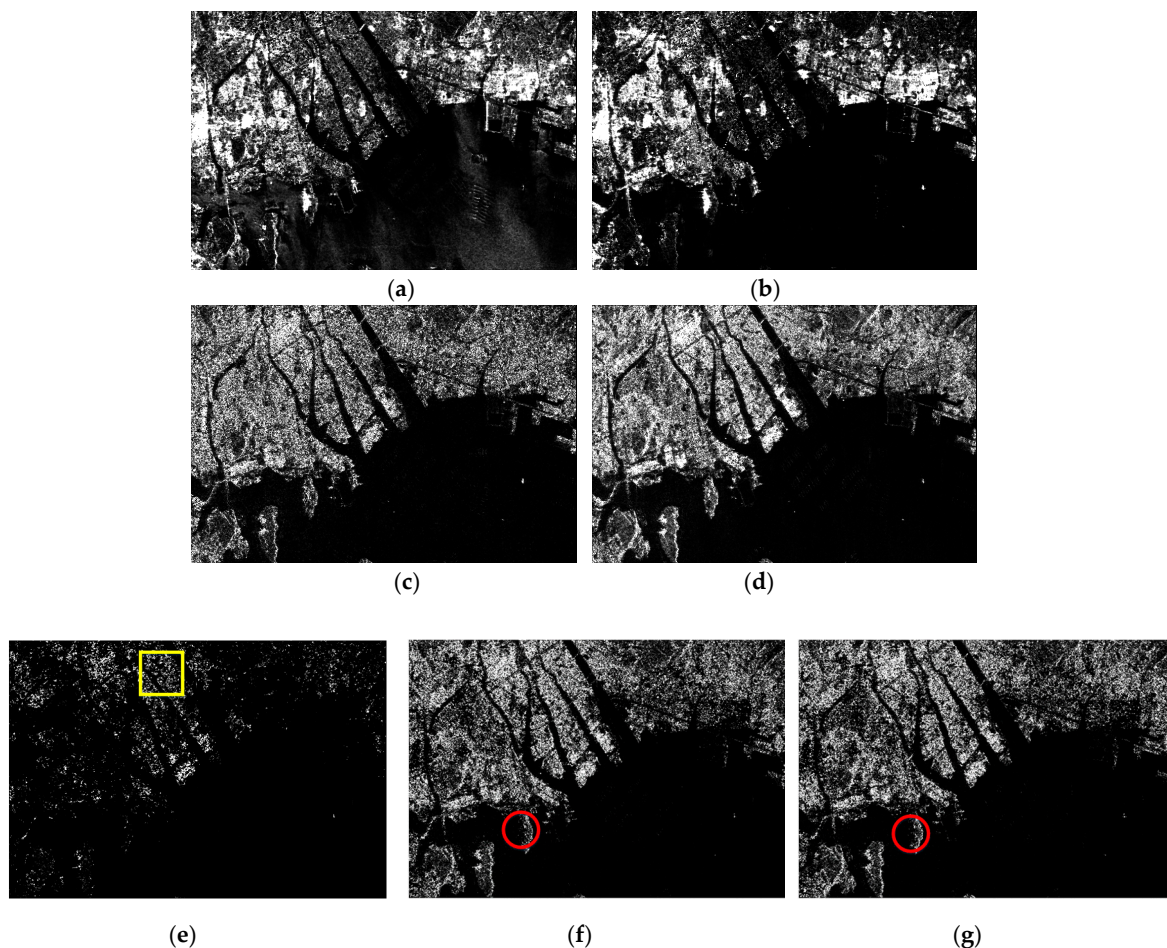


**Figure 5.** The decomposed seven scattering components from the proposed method. (a–g) Surface, double-bounce, helix, volume, obliquely oriented dihedral (OOD),  $\pm 45^\circ$  oriented dipole (OD), and  $\pm 45^\circ$  oriented quarter-wave reflector (OQW) scattering components, respectively.

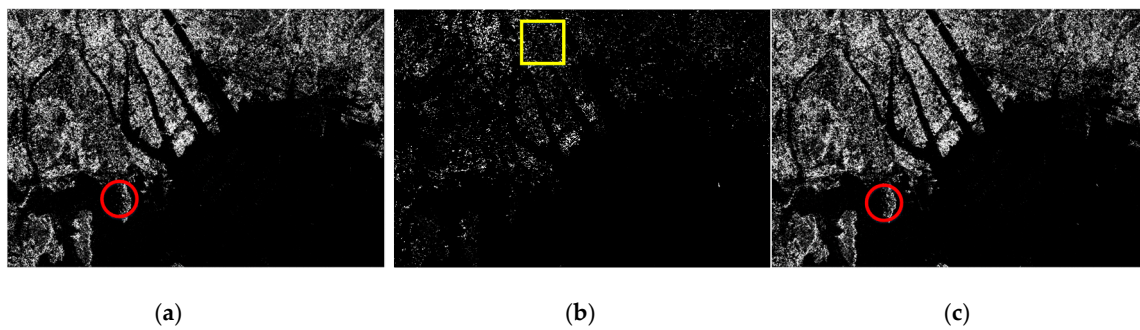


**Figure 6.** Other similar scattering components. (a) Cross scattering component from the X5D method. (b,c)  $\pm 45^\circ$  OD and  $\pm 45^\circ$  OQW scattering components from the 6SD method, respectively.

As mentioned before, the  $\pm 45^\circ$  OD and  $\pm 45^\circ$  OQW scattering exist widely in OOBs, and their contributions are calculated according to the real and imaginary parts of the  $T_{13}$  term. However, comparing the S6D with the proposed method, one can notice that the proportions of these two scattering components are not equal. The difference is that the decomposition procedure in the S6D is implemented after the OAC, while the OAC is not adopted in the proposed method. Despite this, it is difficult to describe their changing trends since the change of  $T_{13}$  term after the OAC is uncertain [15]. Regarding the volume scattering, it can be observed that the proportion in the proposed method is smaller than the one in the S6D. On the one hand, the OOD scattering has already taken up a certain proportion, explaining that the OOD scattering model can effectively characterize the cross-polarization responses. On the other hand, the proposed method still outperforms the S6D in reducing the volume scattering although the S6D applies the OAC to minimize the cross-polarization power. As can be seen, the urban scattering in the proposed method is the highest among all the compared methods; thus, the proposed method provides more accurate interpretation ability. This indicates that rather than from the mathematical perspective, scattering modeling from the physical perspective is more reasonable and effective in improving the OVS.

In summary, the unicity of the proposed seven-component decomposition reflects in the following aspects. First, the proposed method not only highlights and preserves the  $\pm 45^\circ$  OD and  $\pm 45^\circ$  OQW scattering components but also remarkably increases the cross-polarization powers in OOBs via the OOD scattering model. Second, the proposed method elaborately designs the strategies of modular calculation, quadratic discriminant with root determination, and power constraint to fulfill the estimation of scattering contribution. In this case, the OVS is significantly reduced and more reasonable surface scattering is enhanced. Last but not most important, the proposed method can simultaneously decompose seven scattering components, which cannot be processed by any current methods. This provides a unique physical interpretation of target scattering.

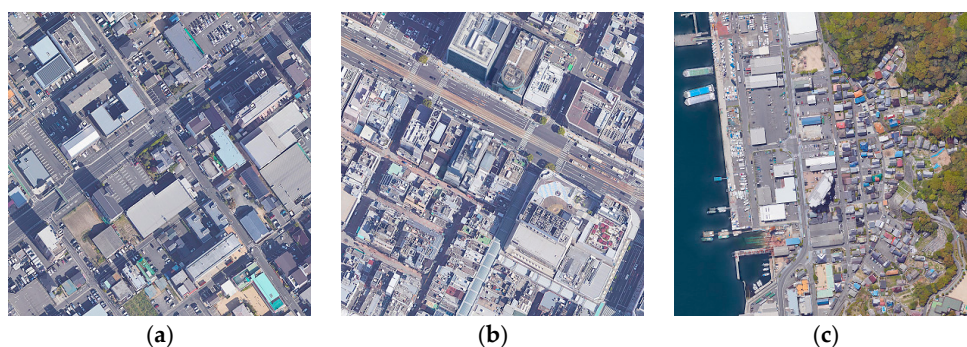


**Figure 7.** Topologies of the selected urban regions. (a–c) Region A–C, respectively.

**Table 1.** Scattering Power Statistics for Region A.

	<b>Proposed</b>	<b>S6D</b>	<b>5SD</b>	<b>S4R</b>	<b>Y4D</b>
Surface scattering	25.59%	24.54%	14.77%	13.48%	12.85%
Double-bounce scattering	6.87%	9.10%	5.00%	5.67%	2.19%
Volume scattering	38.51%	50.62%	71.03%	74.31%	78.41%
Helix scattering	6.55%	6.55%	6.55%	6.55%	6.55%
OOD/Cross scattering	4.68%	—	2.65%	—	—
±45° OD scattering	9.45%	9.43%	—	—	—
±45° OQW scattering	8.73%	8.57%	—	—	—
Urban scattering	36.28%	33.65%	14.2%	12.22%	8.74%

**Table 2.** Scattering Power Statistics for Region B.

	<b>Proposed</b>	<b>S6D</b>	<b>5SD</b>	<b>S4R</b>	<b>Y4D</b>
Surface scattering	18.95%	16.26%	17.59%	16.93%	9.34%
Double-bounce scattering	17.39%	20.34%	15.99%	17.50%	6.06%
Volume scattering	32.03%	36.24%	54.99%	58.40%	77.43%
Helix scattering	7.17%	7.17%	7.17%	7.17%	7.17%
OOD/Cross scattering	5.18%	—	4.27%	—	—
±45° OD scattering	11.63%	12.51%	—	—	—
±45° OQW scattering	7.65%	7.48%	—	—	—
Urban scattering	49.02%	47.5%	27.43%	24.67%	13.23%

### 3.3. Further Validation on C-Band Data

Next, the Radarsat-2 C-band data is applied to further validate the effectiveness of the proposed method. The color composite results of different methods are shown in Figure 8, where the red channel denotes urban scattering (the sum of double-bounce, helix, the OOD/cross scattering, the ±45° OD, and the OQW scattering), the green channel denotes volume scattering, and the blue channel denotes surface scattering. As can be observed, the dominant scattering mechanism in the ocean area is surface scattering, while the AABs are identified to have the double-bounce scattering as dominant. On comparing Figure 8e with other subfigures, it is apparent that the results in OOBs generated by the proposed method appear yellow rather than green, which means that there exists remarkable urban scattering and less volume scattering. This can also be referred to the color of the bridge, as pointed out by the red arrows.

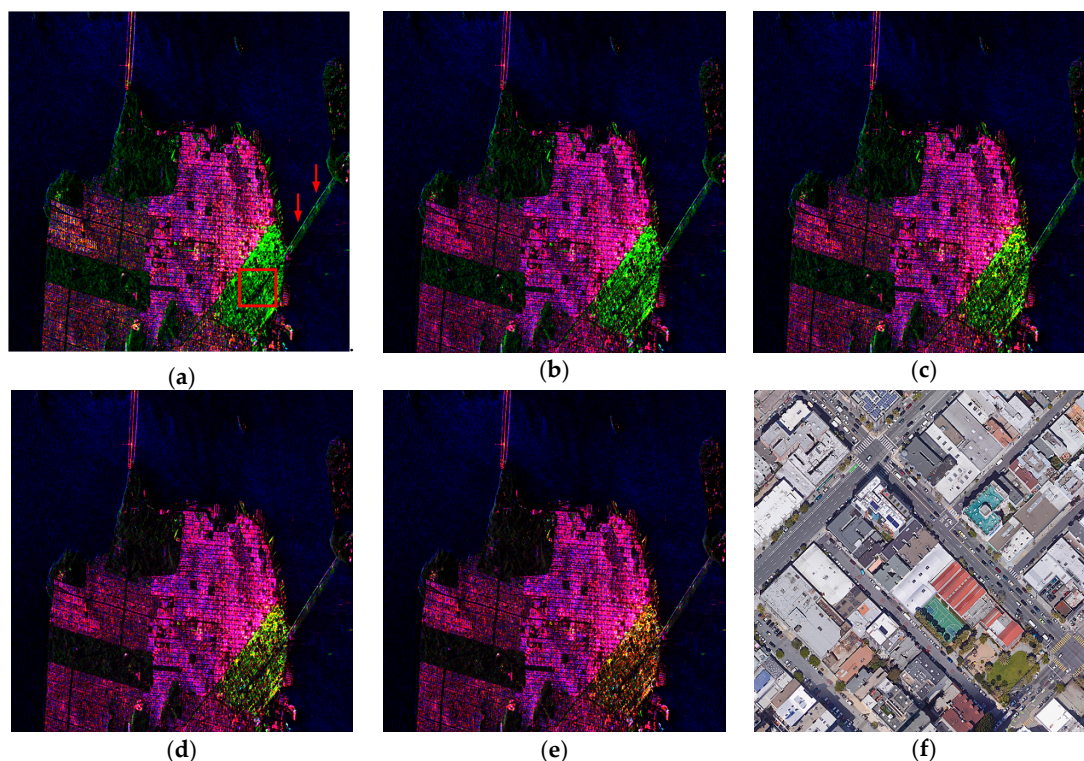


**Figure 8.** Decomposition results for C-band data. (a–e) Color composite results of the Y4D, S4R, X5D, S6D, and the proposed method (red: urban scattering, green: volume scattering, blue: surface scattering). (f) Topologies of the red rectangle region.

To quantify the results, a high-rise OOB region, which tilted by about  $37^\circ$  from the flight trajectory [29] (outlined by the red rectangle), was selected, and the corresponding normalized scattering power statistics are shown in Table 3.

**Table 3.** Scattering Power Statistics for OOBs.

	Proposed	S6D	5SD	S4R	Y4D
Surface scattering	12.29%	6.50%	4.55%	4.55%	3.45%
Double-bounce scattering	14.84%	6.49%	3.53%	5.21%	0.83%
Volume scattering	24.23%	48.68%	59.21%	77.59%	83.09%
Helix scattering	12.63%	12.63%	12.63%	12.63%	12.63%
OOD/Cross scattering	13.79%	—	20.08%	—	—
$\pm 45^\circ$ OD scattering	12.50%	14.72%	—	—	—
$\pm 45^\circ$ OQW scattering	9.72%	10.98%	—	—	—
Urban scattering	63.48%	44.82%	36.24%	17.84%	13.46%

The topologies of this region are shown in Figure 8f. Similar to the aforementioned observation, the helix scattering remains unchanged. The proportions of  $\pm 45^\circ$  OD and  $\pm 45^\circ$  OQW scattering are not equal, and it is hard to describe their changing trends before and after the OAC. With respect to the OOD scattering, its proportion is slightly smaller than that of cross scattering (13.79% versus 20.08%). The reason is that the cross-polarization power in this region is intense while the  $\pm 45^\circ$  OD

and  $\pm 45^\circ$  OQW scattering partake a certain amount of it. In addition, it can be seen that the proportion of double-bounce scattering of the S6D is smaller than that of the proposed method. This can be explained that the OAC loses its effectiveness when the OA is larger than  $22.5^\circ$  [33]. Moreover, it is apparent that the proposed method outperforms other methods in improving the OVS and enhancing the surface scattering of OOBs. Specifically, the volume scattering contributions by the proposed method are decreased by 24.45%, 34.98%, 53.36%, and 58.86%, respectively. These conclusions agree well with those from L-band decomposition, which further validate the robustness and effectiveness of the proposed method.

## 4. Discussions

### 4.1. Comparison of the OOD and the Cross Scattering Models

In order to intuitively compare the proposed OOD scattering model with the CSM, we use a coherency matrix extracted from an OOB pixel to illustrate. The values of coherency matrix elements are shown in Table 4. Using the coherency matrix, the normalized element values of the CSM, and the OOD scattering models are calculated and presented in Table 5.

**Table 4.** Values of Coherency Matrix Elements from an OOB Pixel.

Coherency Matrix Element	$T_{11}$	$T_{22}$	$T_{33}$	$T_{12}$	$T_{13}$	$T_{23}$
Value	0.3558	0.1280	0.3317	0.0152 −0.0104i	−0.0368 −0.0713i	−0.0965 −0.0513i
Actual Proportion ( $T_{33}/T_{22}$ )			2.59			

**Table 5.** Element Values of the Normalized Scattering Models.

Scattering Model	$T_{22}$	$T_{33}$	Proportion ( $T_{33}/T_{22}$ )
Cross Scattering Model	0.5242	0.4758	0.91
OOD Scattering Model	0.3116	0.6884	2.21

To further verify the superiority of the proposed OOD scattering model, we incorporated it into the five-component decomposition scheme and compared the corresponding OOD scattering component with cross scattering component in Figure 9.

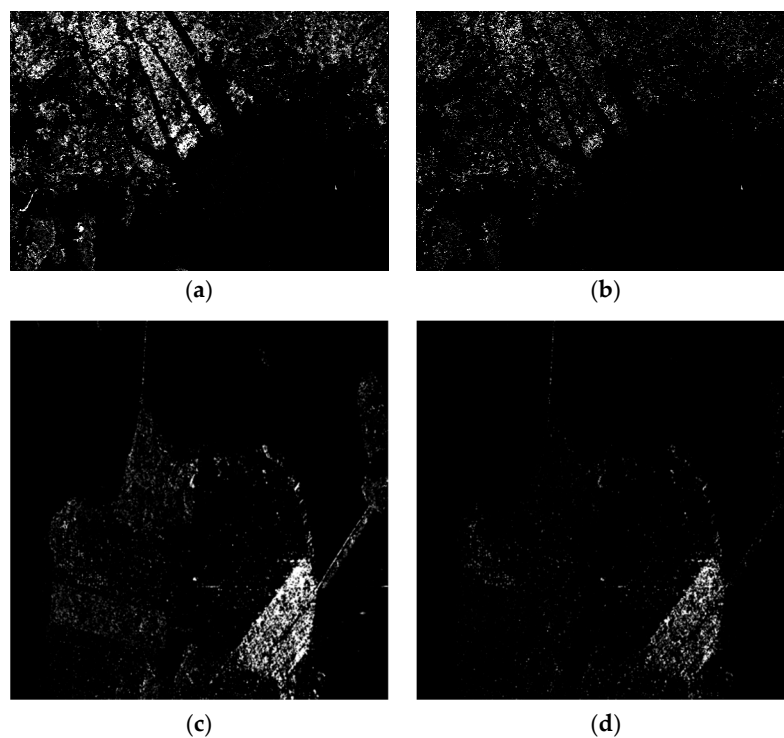


**Figure 9.** Comparison of the OOD scattering model and cross scattering model with five-component decomposition scheme. (a,c) OOD scattering component. (b,d) Cross scattering component.

As can be seen, the cross-polarization component (0.3317) is significantly larger than the co-polarization component (0.1280) according to the coherency matrix (the actual proportion is 2.59). However, the co-polarization component (0.5242) approximates to the cross-polarization component (0.4758) with respect to the CSM (the derived proportion is 0.91). Whereas for the proposed OOD scattering model, the derived relationship between the cross-polarization component (0.6884) and the co-polarization component (0.3116) indicates that it conforms more closely to reality (the derived proportion is 2.21) and provides a more effective way to represent the actual proportions of co-polarization and cross-polarization components in OOBs.

As expected, the cross-scattering components are significant in OOBs and negligible for other land covers. However, in general, cross scattering powers stay at a relatively low level for most OOBs except for some special OOBs. This may increase the risk of the emergence of the OVS. Meanwhile, it can be observed that the OOD scattering model generates more satisfactory results where almost all OOBs are highlighted. Moreover, the OOD scattering model is able to detect more and smaller OOB regions. These signify that the OOD scattering model is more efficient and valid in depicting urban scattering.

#### 4.2. Performance of the Modified Factor

To better justify the definition and provide a physical interpretation of the modified factor  $F_{\text{OOD}}$ , we display the values of  $F_{\text{OOD}}$  in Figure 10.

It is apparent that OOBs are colored brown while AABs and natural land covers are represented by blue tones. This demonstrates that the modified factor can remarkably highlight the scattering characteristics of OOBs while suppressing those of AABs and natural land covers. Moreover, the distributions of brown tones commendably outline the topological structures (shapes and sizes) of OOBs. In addition to these, a pixel with a darker color (i.e., a higher value) indicates that it more likely belongs to an OOB, and its scattering process has more intense depolarization and randomness, as well as less intense polarimetric asymmetry.

Through combining the polarimetric properties of depolarization, randomness, and polarimetric asymmetry, the modified factor  $F_{\text{OOD}}$  actually serves as a robust and effective scattering feature, which

gives a considerable scattering representation of OOBs. Thus, it is applicable for the optimization to derive the OOD scattering model.

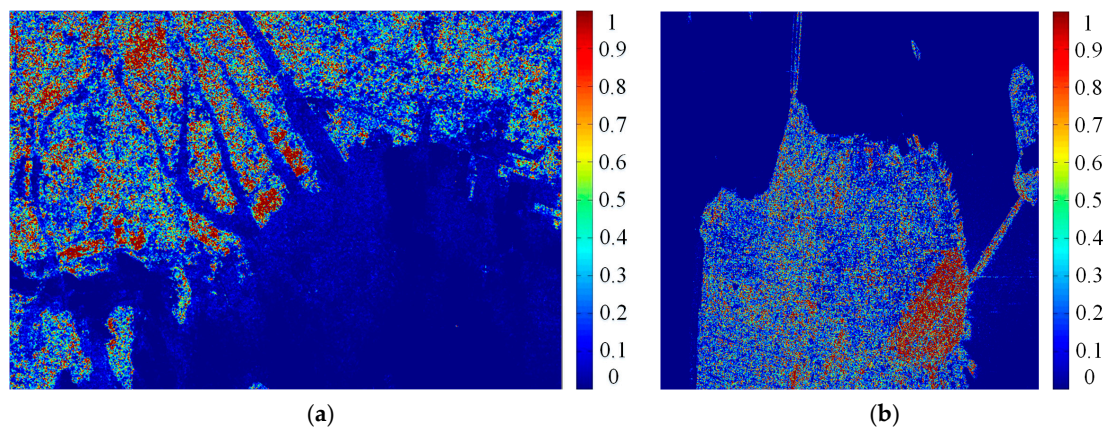


**Figure 10.** The modified factor whose value spans from 0 to 1. (a) L-band data. (b) C-band data.

## 5. Conclusions

Traditional MBD methods suffer the deficiencies of inappropriate and incomprehensive scattering modeling for PolSAR image understanding. In this paper, we propose a seven-component model-based decomposition scheme by integrating three sophisticated scattering models. On the one hand, the OOD scattering model is constructed by modifying the matrix elements of the CSM according to the actual proportions of co-polarization and cross-polarization components. On the other hand, regarding the interpretation of the T13 term in the coherency matrix and for the purpose of utilization of polarimetric information, the  $\pm 45^\circ$  OD and  $\pm 45^\circ$  OQW scattering models are adopted, which are derived from the combination of basic dipoles located at different distances. On this basis, an exquisite model solution strategy is designed to estimate the scattering contributions. Experimental results conducted on different PolSAR data demonstrate that the proposed method outperforms other state-of-the-art MBD methods in significantly reducing the OVS and releasing the reflection symmetry restriction. More importantly, the proposed method helps to understand the target scattering in a more physical manner.

**Author Contributions:** H.F. is responsible for the design of the methodology and the preparation of the paper. S.Q. is responsible for experimental data collection and processing. D.D. and S.X. helped analyze and discuss the results. X.W. is responsible for the technical support of the paper. Conceptualization, H.F. and S.Q.; Methodology, H.F.; Software, S.Q.; Validation, H.F. and S.Q.; Formal Analysis, X.W.; Investigation, D.D.; Resources, S.X.; Data Curation, D.D.; Writing—Original Draft Preparation, H.F.; Writing—Review & Editing, S.Q.; Visualization, H.F. and S.Q.; Supervision, S.X.; Project Administration, X.W.; Funding Acquisition, D.D.

**Funding:** This work is supported by the National Natural Science Foundation of China under Grant 61490693 and the Excellent Youth Foundation Hunan Scientific Committee under Grant No.2017JJ1006.

**Conflicts of Interest:** The authors declare no conflict of interest.

## References

1. Freeman, A.; Durden, S.L. A three-component scattering model for polarimetric SAR data. *IEEE Trans. Geosci. Remote Sens.* **1998**, *36*, 963–973. [[CrossRef](#)]
2. Yamaguchi, Y.; Moriyama, T.; Ishido, M.; Yamada, H. Four-component scattering model for polarimetric SAR image decomposition. *IEEE Trans. Geosci. Remote Sens.* **2005**, *43*, 1699–1706. [[CrossRef](#)]
3. Quan, S.; Xiang, D.; Xiong, B.; Hu, C.; Kuang, G. A Hierarchical Extension of General Four-Component Scattering Power Decomposition. *Remote Sens.* **2017**, *9*, 856. [[CrossRef](#)]
4. Xie, Q.; Ballester-Berman, D.; Lopez-Sanchez, J.M.; Zhu, J.; Wang, C. On the use of generalized volume scattering models for the improvement of general polarimetric model-based decomposition. *Remote Sens.* **2017**, *9*, 117. [[CrossRef](#)]

5. Fan, H.; Quan, S.; Dai, D.; Wang, X.; Xiao, S. Refined Model-Based and Feature-Driven Extraction of Buildings from PolSAR Images. *Remote Sens.* **2019**, *11*, 1379. [[CrossRef](#)]
6. Arii, M.; van Zyl, J.J.; Kim, Y. Adaptive model-based decomposition of polarimetric SAR covariance matrices. *IEEE Trans. Geosci. Remote Sens.* **2010**, *49*, 1104–1113. [[CrossRef](#)]
7. Chen, S.W.; Wang, X.S.; Li, Y.Z.; Sato, M. Adaptive model-based polarimetric decomposition using polinsar coherence. *IEEE Trans. Geosci. Remote Sens.* **2013**, *52*, 1705–1718. [[CrossRef](#)]
8. Bhattacharya, A.; Singh, G.; Manickam, S.; Yamaguchi, Y. An adaptive general four-component scattering power decomposition with unitary transformation of coherency matrix (AG4U). *IEEE Geosci. Remote Sens. Lett.* **2015**, *12*, 2110–2114. [[CrossRef](#)]
9. Zou, B.; Zhang, Y.; Cao, N.; Minh, N.P. A four-component decomposition model for PolSAR data using asymmetric scattering component. *IEEE J. Sel. Topics Appl. Earth Observ. Remote Sens.* **2015**, *8*, 1051–1061. [[CrossRef](#)]
10. Yajima, Y.; Yamaguchi, Y.; Sato, R.; Yamada, H.; Boerner, W.M. POLSAR image analysis of wetlands using a modified four-component scattering power decomposition. *IEEE Trans. Geosci. Remote Sens.* **2008**, *46*, 1667–1673. [[CrossRef](#)]
11. Krogager, E. Aspects of Polarimetric Radar Imaging. Doctoral Thesis, Technical University of Denmark, Copenhagen, Denmark, 1993.
12. Van Zyl, J.J.; Arii, M.; Kim, Y. Model-based decomposition of polarimetric SAR covariance matrices constrained for nonnegative eigenvalues. *IEEE Trans. Geosci. Remote Sens.* **2011**, *49*, 3452–3459. [[CrossRef](#)]
13. Cui, Y.; Yamaguchi, Y.; Yang, J.; Kobayashi, H.; Park, S.E.; Singh, G. On complete model-based decomposition of polarimetric SAR coherency matrix data. *IEEE Trans. Geosci. Remote Sens.* **2013**, *52*, 1991–2001. [[CrossRef](#)]
14. Lim, Y.X.; Burgin, M.S.; van Zyl, J.J. An optimal nonnegative eigenvalue decomposition for the Freeman and Durden three-component scattering model. *IEEE Trans. Geosci. Remote Sens.* **2017**, *55*, 2167–2176. [[CrossRef](#)]
15. Lee, J.S.; Ainsworth, T.L. The effect of orientation angle compensation on coherency matrix and polarimetric target decompositions. *IEEE Trans. Geosci. Remote Sens.* **2011**, *49*, 53–64. [[CrossRef](#)]
16. Chen, S.W.; Wang, X.S.; Xiao, S.P.; Sato, M. General polarimetric model-based decomposition for coherency matrix. *IEEE Trans. Geosci. Remote Sens.* **2013**, *52*, 1843–1855. [[CrossRef](#)]
17. Maurya, H.; Panigrahi, R.K. Polsar coherency matrix optimization through selective unitary rotations for model-based decomposition scheme. *IEEE Geosci. Remote Sens. Lett.* **2018**, *16*, 658–662. [[CrossRef](#)]
18. An, W.; Xie, C.; Yuan, X.; Cui, Y.; Yang, J. Four-component decomposition of polarimetric SAR images with deorientation. *IEEE Geosci. Remote Sens. Lett.* **2011**, *8*, 1090–1094. [[CrossRef](#)]
19. Singh, G.; Yamaguchi, Y.; Park, S.E. General four-component scattering power decomposition with unitary transformation of coherency matrix. *IEEE Trans. Geosci. Remote Sens.* **2012**, *51*, 3014–3022. [[CrossRef](#)]
20. Sato, A.; Yamaguchi, Y.; Singh, G.; Park, S.E. Four-component scattering power decomposition with extended volume scattering model. *IEEE Geosci. Remote Sens. Lett.* **2011**, *9*, 166–170. [[CrossRef](#)]
21. Zhang, L.; Zou, B.; Cai, H.; Zhang, Y. Multiple-component scattering model for polarimetric SAR image decomposition. *IEEE Geosci. Remote Sens. Lett.* **2008**, *5*, 603–607. [[CrossRef](#)]
22. Xiang, D.; Ban, Y.; Su, Y. Model-based decomposition with cross scattering for polarimetric SAR urban areas. *IEEE Geosci. Remote Sens. Lett.* **2015**, *12*, 2496–2500. [[CrossRef](#)]
23. Singh, G.; Yamaguchi, Y. Model-based six-component scattering matrix power decomposition. *IEEE Trans. Geosci. Remote Sens.* **2018**, *56*, 5687–5704. [[CrossRef](#)]
24. Atwood, D.K.; Thirion-Lefevre, L. Polarimetric phase and implications for urban classification. *IEEE Trans. Geosci. Remote Sens.* **2018**, 1–12. [[CrossRef](#)]
25. Quan, S.; Xiang, D.; Xiong, B.; Kuang, G. Derivation of the Orientation Parameters in Built-up Areas: With Application to Model-based Decomposition. *IEEE Trans. Geosci. Remote Sens.* **2018**, *56*, 4714–4730. [[CrossRef](#)]
26. Xiang, D.; Tang, T.; Ban, Y.; Su, Y.; Kuang, G. Unsupervised polarimetric SAR urban area classification based on model-based decomposition with cross scattering. *ISPRS J. Photogramm. Remote Sens.* **2016**, *116*, 86–100. [[CrossRef](#)]
27. Hong, S.H.; Wdowinski, S. Double-bounce component in cross-polarimetric SAR from a new scattering target decomposition. *IEEE Trans. Geosci. Remote Sens.* **2013**, *52*, 3039–3051. [[CrossRef](#)]
28. Li, H.; Li, Q.; Wu, G.; Chen, J.; Liang, S. The impacts of buildings orientation on polarimetric orientation angle estimation and model-based decomposition for multilook polarimetric SAR data in urban areas. *IEEE Trans. Geosci. Remote Sens.* **2016**, *54*, 5520–5532. [[CrossRef](#)]

29. Quan, S.; Xiong, B.; Xiang, D.; Hu, C.; Kuang, G. Scattering characterization of obliquely oriented buildings from PolSAR data using eigenvalue-related model. *Remote Sens.* **2019**, *11*, 581. [[CrossRef](#)]
30. Quan, S.; Xiong, B.; Xiang, D.; Zhao, L.; Zhang, S.; Kuang, G. Eigenvalue-based urban area extraction using polarimetric SAR data. *IEEE J. Sel. Topics Appl. Earth Observ. Remote Sens.* **2018**, *11*, 458–471. [[CrossRef](#)]
31. Lee, J.S.; Pottier, E. *Polarimetric Radar Imaging: From Basics to Applications*; Taylor Francis: Boca Raton, FL, USA, 2009; pp. 85–158. ISBN 9781420054972.
32. Cloude, S.R. *Polarisation: Applications in Remote Sensing*; Oxford University Press: New York, NY, USA, 2010; pp. 57–65. ISBN 9780191574382.
33. Chen, S.W.; Ohki, M.; Shimada, M.; Sato, M. Deorientation effect investigation for model-based decomposition over oriented built-up areas. *IEEE Geosci. Remote Sens. Lett.* **2013**, *10*, 273–277. [[CrossRef](#)]



© 2019 by the authors. Licensee MDPI, Basel, Switzerland. This article is an open access article distributed under the terms and conditions of the Creative Commons Attribution (CC BY) license (<http://creativecommons.org/licenses/by/4.0/>).